Large spin Hall effect in an amorphous binary alloy

Katharina Fritz,[1] Sebastian Wimmer,[2] Hubert Ebert,[2] and Markus Meinert[1,*]

[1]*Center for Spinelectronic Materials and Devices, Department of Physics, Bielefeld University, D-33501 Bielefeld, Germany*
[2]*Department Chemie, Physikalische Chemie, Ludwig-Maximilians-Universität München, D-81377 Munich, Germany*

We investigate the spin Hall effect of W-Hf thin films, which exhibit a phase transition from a segregated phase mixture to an amorphous alloy below 70% W. The spin Hall angle was determined with a planar harmonic Hall voltage technique. Due to the accompanying jump in resistivity, the spin Hall angle shows a pronounced maximum at the composition of the phase transition. The spin Hall conductivity does, however, reduce from W to Hf with a weak discontinuity across the phase transition. The maximum spin Hall angle of $\theta_{SH} = -0.20$ is obtained for amorphous $W_{0.7}Hf_{0.3}$. A detailed comparison with spin Hall conductivities calculated from first principles for hcp, fcc, and bcc solid solutions provides valuable insight into the alloying physics of this binary system.

I. INTRODUCTION

The spin Hall effect [1–4] converts a charge current density j into a transverse spin current density j_s. The charge-to-spin conversion efficiency is characterized by the spin Hall angle (SHA) $\theta_{SH} = j_s/j$. Effects from the band structure (intrinsic) as well as extrinsic effects from scattering (skew scattering and side-jump scattering) contribute to the spin Hall angle. In the dilute limit, the intrinsic and side-jump contributions to the SHA depend on the resistivity, whereas the skew-scattering contribution is independent of the resistivity, i.e., $\theta_{SH} = \tilde{\sigma}_{SH}\rho_{xx} + b$, where $\tilde{\sigma}_{SH}$ is the sum of intrinsic and side-jump spin Hall conductivity. Assuming the skew-scattering contribution to be negligible, i.e., for high impurity concentration, the SHA can be rewritten as $\theta_{SH} = \tilde{\sigma}_{SH}/\sigma_{xx}$. The spin Hall conductivity (SHC) of crystalline materials is both experimentally [5–9] and theoretically [10–14] well understood and various metals with large spin Hall conductivity were identified, such as Pt [6], β-W [15], and β-Ta [16]. The scaling relation between resistivity and spin Hall angle was experimentally verified for Pt thin films [6]. This scaling also explains the large range of reported SHAs in the literature for a single material [4]. By doping Pt with Au, Al, or Hf, it was shown that the resistivity can be increased and that the spin Hall angle can be tuned by alloying [17,18]. The spin current originating from the spin Hall effect can be absorbed by an adjacent ferromagnetic layer, where the angular momentum transfer gives rise to so-called spin-orbit torques [19]. These may induce precession of the magnetization [20], domain wall motion [21], or switching of the magnetization orientation [15,16,22]. Various concepts for spin Hall based magnetic memory devices, e.g., the so-called spin-orbit torque magnetic random access memory (SOT-MRAM), were proposed [23–26], which hold promise for a more energy efficient and

enduring memory cell as compared to spin-transfer torque (STT-)MRAM and even to conventional SRAM [27,28].

Tungsten is the element with the largest negative spin Hall conductivity [10]. While the bcc phase of W has a low resistivity and thus a small SHA, the β phase of W typically has a high resistivity and thus an exceptionally high SHA up to -0.5, which was achieved by oxygen incorporation into the material [29]. However, due to the metastability of the β-W, this material is unsuitable for applications that require high-temperature annealing [30]. In the present work, we attempt to create a high-resistivity binary alloy thin film based on W by mixing with Hf. The binary phase diagram [31] contains a line compound at the stoichiometry W_2Hf with the cubic Laves structure (C15). Across the full range of composition, phase mixtures of bcc-W + W_2Hf or hcp-Hf + W_2Hf are expected with negligible mutual solubility at low temperature. We thus expect to obtain phase-segregated films with small grains and high resistivity and therefore large spin Hall angle. Instead, we discover an amorphous phase over a broad composition range which has both a high SHA and SHC.

II. METHODS

A. Experiment

Thin films of W-Hf were grown by dc magnetron cosputtering on thermally oxidized Si wafers at room temperature. The full stack was Si (001) / SiO_x 50 nm / W_xHf_{1-x} 8 nm / $Co_{40}Fe_{40}B_{20}$ 3 nm / TaO_x 2 nm. The growth rates of Hf and W were determined by an x-ray reflectivity to determine the power ratios of the W and Hf sources for the stoichiometry series. The Ar working pressure was 2×10^{-3} mbar and the base pressure of the deposition system was 5×10^{-9} mbar. The alloy film thicknesses were confirmed by x-ray reflectivity. X-ray diffraction with Cu K_α radiation was performed in a diffractometer with Bragg-Brentano geometry. The film resistivities were determined by a four-probe technique with four equidistant needles in a line, such that the effective resistivity of the multilayer can be written as $\rho_{xx}^{ML} = \frac{\pi}{\ln 2}\frac{U}{I}(t_{W_xHf_{1-x}} + $

*meinert@physik.uni-bielefeld.de

t_{CFB}). A parallel circuit model was subsequently applied with $\rho_{CFB} = 175 \times 10^{-8} \ \Omega$ m as determined for a 3 nm CFB film to obtain the alloy resistivity ρ_{xx}.

For the determination of the spin Hall angle, the films were patterned into fourfold rotationally symmetric Hall crosses with a conductor width of $w = 16 \ \mu$m and a length of $l = 48 \ \mu$m by optical lithography. Harmonic Hall voltage measurements were performed in a dual Halbach cylinder array with a rotating magnetic field up to 1.0 T (MultiMag, Magnetic Solutions Ltd.). A current density with a rms value of $j_{rms} = 2 \times 10^{10}$ A/m^2 ($I_{rms} = 3.52$ mA) was injected into the Hall crosses and the in-phase first harmonic and out-of-phase second harmonic Hall voltages were recorded simultaneously upon in-plane field rotation with a Zurich Instruments MFLI multidemodulator lock-in amplifier.

The second harmonic out-of-phase Hall voltage rms value $V_{2\omega}$ can be written as [32–34]

$$V_{2\omega} = \left(-\frac{B_{FL}}{B_{ext}} R_P \cos 2\varphi - \frac{1}{2} \frac{B_{DL}}{B_{eff}} R_A + \alpha' I_0 \right) I_{rms} \cos\varphi. \tag{1}$$

The angle φ is the in-plane angle between current and magnetization and $B_{eff} = B_{ext} + B_{sat}$ is the effective field. The out-of-plane saturation field $B_{sat} = B_{dem} - B_{ani} > 0$ and the anomalous Hall resistance amplitude R_A were obtained from Hall voltage measurements in a perpendicular magnetic field up to 2.2 T. The planar Hall amplitudes R_P were obtained from the first harmonic $V_\omega = R_P I_{rms} \sin 2\varphi$. B_{FL} and B_{DL} are the current-induced effective field amplitudes associated with the fieldlike (FL) and dampinglike (DL) spin-orbit torques [35]. Here it is assumed that in-plane anisotropy fields (uniaxial, biaxial, etc.) are negligibly small compared to the external magnetic field and can be neglected. The term $\alpha' I_0$ describes a parasitic contribution arising from the anomalous Nernst effect (ANE), which yields an electric field $\boldsymbol{E}_{ANE} = -\alpha \nabla T \times \boldsymbol{m} \propto I_0^2$, where I_0 is the current amplitude. The prefactor α' summarizes all geometrical parameters and the film resistivity, heat conductivity, etc. that determine ∇T. In some samples a weak unixial anisotropy was observed with $B_U \ll B_{ext}$ for the typical external fields used here. Therefore, usage of formula 1 is well justified. The formula was fitted to the experimental data and dampinglike effective fields and anomalous-Nernst contributions were separated by their dependence on the external field; see Appendix for details [33]. The spin Hall angle was obtained from the dampinglike effective field as

$$\theta_{SH} = \frac{2e}{\hbar} \frac{B_{DL} M_s t_{CFB}}{j_0^{HM}}, \tag{2}$$

where j_0^{HM} is the current density amplitude in the heavy-metal layer far away from the Hall voltage pickup lines. The magnetization of the CoFeB film was determined by alternating gradient magnetometry to be $M_s = (1100 \pm 50)$ kA/m. The parallel circuit model was applied to determine the current density flowing in the heavy-metal layer. A correction factor 1.45 for the inhomogeneous current flow in the Hall crosses was applied to the spin Hall angle, as suggested by a recent study on the influence of the aspect ratio of the Hall cross on the effective field determination [36].

B. First-principles calculations

The spin Hall conductivities were calculated in a fully relativistic multiple-scattering Green function framework using the Kubo-Bastin formalism [12]. Intrinsic and extrinsic contributions to the spin Hall conductivity are treated on equal footing. Furthermore, chemical alloying as well as temperature-induced disorder are accounted for within the coherent potential approximation (CPA) or the alloy-analogy model (AAM) [37], respectively. The formalism is implemented in the Munich Spin-Polarized Relativistic Korringa-Kohn-Rostoker (SPR-KKR) program package [38,39]. The Green function was expanded up to $\ell_{max} = 3$ and the Fermi energy was accurately obtained with Lloyd's formula. The atomic sphere approximation (ASA) was used throughout. For the evaluation of the Kubo-Bastin formula 32 points were used for the energy integration. Approximately 5×10^7 k-points in the full Brillouin zone were used to ensure an accurate evaluation of the Brillouin zone integrals for the Fermi surface term. The spin Hall conductivities were calculated for bcc, fcc, and hcp solid solutions, where the atomic volumes and the Debye temperatures are interpolated between the experimental values according to Vegard's rule. Additionally, the spin Hall conductivity of W$_2$Hf (C15 Laves phase) was calculated using experimental lattice constants. The spin Hall conductivities were calculated at 300 K in all cases. In addition, alloy formation energies per atom ΔE were calculated as

$$\Delta E_\alpha(x) = E_\alpha(W_x Hf_{1-x}) - [x E_{bcc}(W) + (1-x) E_{hcp}(Hf)], \tag{3}$$

where $\alpha = $ fcc, bcc, hcp and E_α represents the elemental total energies per atom.

III. STRUCTURAL CHARACTERIZATION

In Fig. 1(a) we show x-ray diffraction patterns of our stoichiometry series. In the W-rich portion down to 72% W, a diffraction peak is found that can be indexed as bcc-W (110), in agreement with the expectation that bcc-W will grow with a strong (110) preferred growth direction on SiO$_x$ to minimize its interface energy. The strong diffraction peak in the pure Hf can be indexed as hcp-Hf (0002) or fcc-Hf (111). Both growth modes are in agreement with minimization of the interface energy. For very small crystallite size ($\lesssim 5$ nm), it was shown that Hf can crystallize in an fcc structure induced by the surface tension of the crystallites [41]. The length of coherent scattering along the growth direction D_z can be determined with Scherrer's formula, $D_z = k\lambda/(B \cos\theta)$, with $k = 0.8$ and B the observed peak full width at half maximum. For the pure Hf film, we obtain a crystallite size of 5 nm; thus the Hf film might be at the verge of the transition between fcc and hcp allotropes. This is supported by the fact that the lattice spacing is intermediate between the values of hcp-Hf (experimental) and fcc-Hf (theoretical). At 100% W, we obtain $D_z \approx 8$ nm, i.e., the film has a fiber texture with grains extending along the full thickness of the film. Additional evidence for the very good crystal quality comes from the presence of symmetric Laue oscillations around the diffraction peak. With increasing Hf content, the peaks become slightly broader and the Laue oscillations vanish. This indicates either a smaller D_z or the
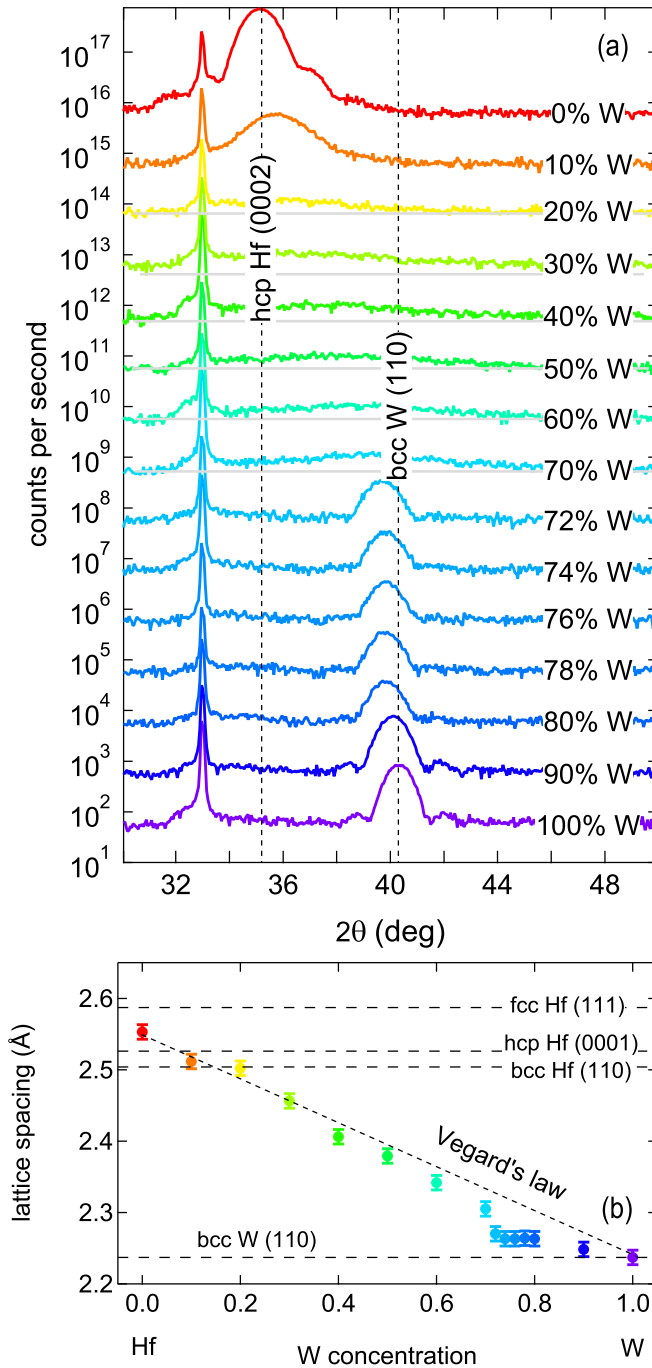
FIG. 1. (a) X-ray diffraction patterns of $W_x Hf_{1-x}$ 8 nm / CoFeB 3 nm / TaO_x 2 nm films. Peaks in the composition range $x = 0.7$–0.2 are weak and broad. Light gray lines are drawn to indicate the background levels and improve the visibility of the amorphous diffraction humps. The color code for the W-Hf stoichiometries is used throughout the article. (b) Lattice spacing obtained from the diffraction peaks. The short-dashed line indicates Vegard's law; the long-dashed lines indicate the lattice spacings of various allotropes as denoted in the graph. The lattice spacings of fcc-Hf and bcc-Hf are theoretical values taken from The Materials Project database [40].

presence of microstrain in the grains, i.e., a change of lattice constant along the growth direction. Simultaneously, the diffraction peaks shift to smaller angles and become slightly broader. In the composition range of $x = 0.2$–0.7, broad

humps are observed, with the position of the humps varying linearly with the stoichiometry. Using Scherrer's formula, $D_z \approx (0.9 \pm 0.2)$ nm is found in this regime. We interpret this as an amorphous phase that has some local order spanning three to four interatomic distances. The observed humps can be interpreted as local atomic arrangements of either bcc (110)-type, hcp (0001)-type, or fcc (111)-type.

In the W-rich part of the series, the interatomic distance d_{hkl} [Fig. 1(b)] does clearly deviate from Vegard's law, according to which it would vary linearly between the lattice spacings of bcc-W and bcc-Hf as a function of the stoichiometry parameter x. In fact, a saturation of the lattice spacing at 2.264 Å is observed. This agrees with the binary phase diagram [31], according to which a mixture of bcc-W and W_2Hf is expected in this regime and essentially no Hf would dissolve in the bcc-W lattice. The crystalline phase seen in the x-ray diffraction is an almost pure bcc-W. The slight expansion of the lattice spacing may be due to a small fraction of Hf dissolved in the bcc-W lattice or may originate from compressive strain caused by Hf or W_2Hf precipitates in the grain boundaries. In either case, we conclude that for $x > 0.7$ no solid solution is formed, whereas the amorphous phase in the range $0.3 \leqslant x \leqslant 0.7$ is a homogenous solution of Hf and W, where the interatomic distance follows Vegard's law. We found no evidence for the formation of crystalline W_2Hf in the thin films.

IV. ELECTRICAL RESISTIVITY AND SPIN HALL CONDUCTIVITY

The electrical resistivity shows clear signs of the phase transition, as is shown in Fig. 2(a). Upon Hf addition into W, the resistivity is increased linearly, similar to what is expected for a solid solution. At the stoichiometry of the transition, the resistivity jumps by 90%. In the amorphous regime, the resistivity increases up to $W_{0.1}Hf_{0.9}$.

As shown in Fig. 2(b), the spin Hall angle obtained from the planar harmonic Hall measurements resembles the increase of the resistivity in the W-rich films and exhibits a jump at the phase transition. The maximum spin Hall angle of $\theta_{SH} = -0.20$ is obtained at $x = 0.7$. The anomalous Nernst coefficient α', shown in Fig. 2(c), behaves similar to the resistivity. This can be explained by the proportionality of the temperature gradient to the heating power and therefore to the resistivity. The spin Hall conductivity $\sigma_{SH} = \theta_{SH}/\rho_{xx}$ [Fig. 2(d)] shows a nearly linear dependence on the composition irrespective of the phase transition, where only a small discontinuity is seen. The spin Hall conductivity (SHC) of the pure W film is difficult to obtain accurately with CoFeB as the ferromagnet; see the Appendix for details. We find $(-1.35 \pm 0.9) \times 10^5$ S/m, in fair agreement with a theoretical prediction [42]. The SHC at $x = 0.7$ is found to be -1.2×10^5 S/m. In the amorphous regime, a nearly linear decrease of the SHC with increasing Hf content is observed. The SHC of pure Hf is surprisingly found to be positive with a value of 0.15×10^5 S/m. Because of the rather thick films in our experiment, we do not correct for incomplete saturation of the diffusive spin current and assume that the film thickness is well beyond the spin-diffusion length across the whole composition series. We estimate the electron mean-free path
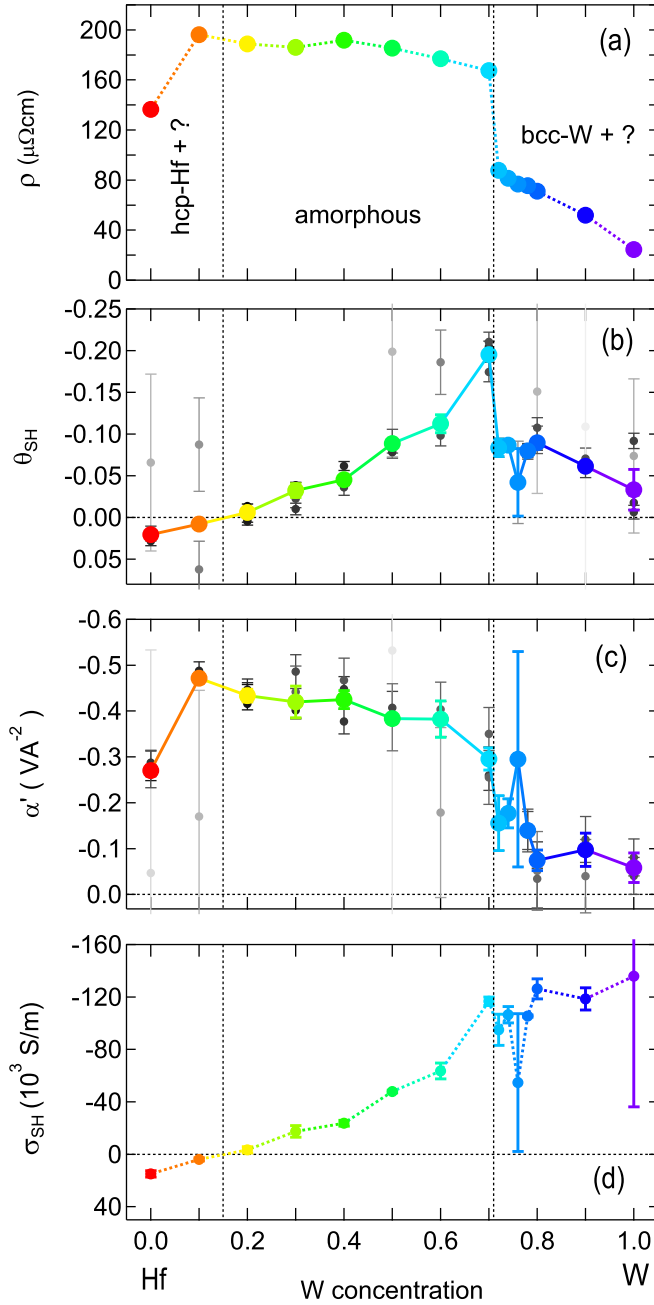
FIG. 2. (a) Resistivity ρ_{xx} of the 8 nm $W_x Hf_{1-x}$ films. (b) Spin Hall angle determined with the planar harmonic Hall method. (c) Anomalous Nernst parameter α' as defined in Eq. (1). (d) Spin Hall conductivity $\sigma_{SH} = \theta_{SH}/\rho_{xx}$. The dashed lines indicate the phase transformations observed in x-ray diffraction. Gray scale data points are obtained on individual Hall crosses; rainbow-colored data points are obtained from inverse-variance weighted averages over three to four Hall crosses. Lighter gray stands for lower weight in the weighted average. Details of the error analysis are given in the Appendix.
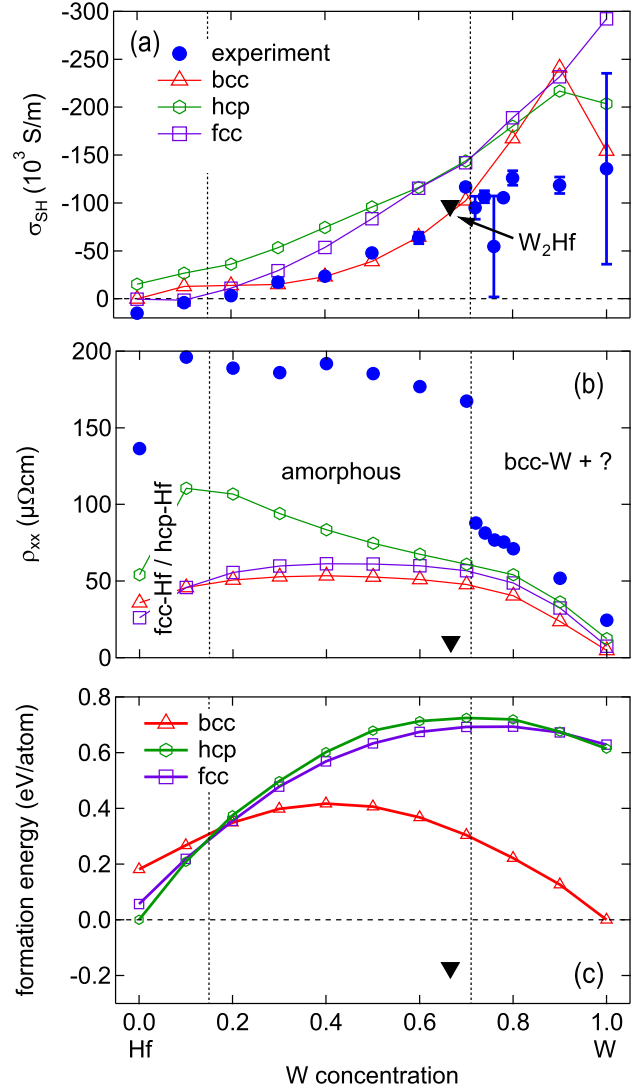

FIG. 3. Comparison of spin Hall conductivity (a) and resistivity (b), for experiment, three alloy models (bcc, hcp, fcc), and W_2Hf (C15) calculated at 300 K. The dashed lines indicate the phase transitions observed in x-ray diffraction. Additionally, the formation energies of the three alloy formation energies and the W_2Hf formation energy are shown in (c).

λ_0 based on a detailed analysis of the resistivity of epitaxial W films in Ref. [43], for which $\rho_0 \lambda_0 = 1.01 \times 10^{-15} \, \Omega \, m^2$ was obtained, with the bulk resistivity ρ_0. In the amorphous phase, $\lambda_0 \approx 5.9 \times 10^{-10}$ m is obtained, i.e., of the order of two interatomic distances, corroborating the amorphous char-

acter of the material. The spin-diffusion length λ_{sf} can be expressed with the spin-flip probability p_{sf} as $\lambda_{sf} = \lambda_0/p_{sf}$. In heavy elements, the spin-flip probability is of the order 0.5 ($p_{sf} = 0.57$ in Pt [6]), so that the spin-diffusion length is estimated to be of the order of $\lambda_{sf} \approx 1$ nm in the amorphous regime. Therefore, the assumption of a saturated spin current is certainly justified in this case. However, strictly speaking, the spin Hall angles and conductivities given here are lower bounds to the true values in the respective bulk material.

To improve the understanding of the SHC in the W-Hf system, we compute it using a fully relativistic implementation of the Kubo-Bastin formalism with the Munich SPR-KKR program package. In Fig. 3 we show a comparison of the experimental SHC and the calculated values for the three Bravais lattices considered. Results are shown including the

so-called vertex corrections which, however, are negligible in the considered concentration range. Remarkably, the calculations for the bcc structure predict a sharp peak of the SHC at a composition of $W_{0.9}Hf_{0.1}$. This peak is absent in the experiment, in agreement with the inference from the lattice constant analysis that no solid solution is formed in the W-rich films. The calculated SHC is larger than the experimental value for pure bcc-W. In the previous section, we argued that two mechanisms can give rise to the peak shift observed in the W-rich part of the series. Based on the SHC data, we rule out the possibility of large amounts of Hf dissolving in the bcc-W lattice, because in this case a strongly enhanced SHC should be observed. The approximately constant SHC in the W-rich regime can be understood by considering two counteracting effects: a small amount of Hf can dissolve in bcc-W, giving rise to an increase of the SHC, while the fraction of bcc-W reduces linearly with increased Hf content. Our results are thus consistent with less than 10% Hf dissolved in W, while the remainder stays in the grain boundaries. The XRD peak shift is partially due to the lattice expansion by the Hf entering the bcc-W lattice and partially due to compressive strain acting on the bcc-W grains caused by the Hf segregation into the grain boundaries.

The amorphous part of the stoichiometry series is best described by the calculation for the bcc solid solution with (110) texture and near-quantitative agreement between experiment and theory is obtained. The fcc and hcp calculations deviate significantly and are consistently larger than the experimental data. In the Hf-rich portion, the SHC is substantially closer to the fcc calculation than to the hcp calculation, which indicates that the pure Hf film could indeed be in the fcc phase. The calculated resistivities, shown in Fig. 3(b), grossly deviate from the measured data, because only chemical disorder and finite temperature in otherwise perfect crystals is taken into account. Due to the small crystal, interfaces, and short mean-free path in the amorphous phase, the experimental resistivity is much larger than the calculated values. Thus the measured resistivity does not help to identify the phases and local atomic arrangements. In Fig. 3(c) we plot the alloy formation energies for the bcc, fcc, hcp, and W_2Hf phases. In agreement with experimental findings [31], the alloy formation energies are positive, i.e., no solid solutions of W and Hf exist. Only the W_2Hf compound has a negative formation energy and can be synthesized experimentally. We observe that the formation energy for the bcc order is lower than the fcc and hcp formation energies for $x \gtrsim 0.2$. We thus speculate that the amorphous phase, facilitated by the configurational entropy contribution to the free energy of the disordered state, will preferentially exhibit a bcc-type local order. This is consistent with the excellent agreement between the experimental SHC and the bcc calculation. The phase transition from amorphous phase to nanocrystalline fcc-Hf occurs experimentally at the stoichiometry at which the formation energies of both fcc and hcp solutions become smaller than the bcc type, or equivalently, 0.32 eV/atom. In this regime, it remains unclear whether a solution of W and Hf is formed or, alternatively, fcc-Hf crystallites are formed with W precipitates in the grain boundaries. W_2Hf has a negative formation energy and is thus energetically favorable over the solid solutions. However, the structure has 24 atoms

in the cubic cell and is thus, based on our experience with sputter growth of crystalline materials, rather unlikely to form in a deposition process at room temperature. Typically, high growth temperatures or a high-temperature postannealing are required to obtain complex crystalline phases. We therefore conclude that the local atomic arrangement in the amorphous phase is most likely of the bcc type with a preferred (110) orientation, which gives rise to the broad hump in the x-ray diffraction patterns.

V. CONCLUSION

In summary, we obtained a large spin Hall angle up to $\theta_{SH} = -0.20$ in an amorphous W-Hf phase, which has local order with a correlation length of less than 1 nm. We demonstrated that the spin Hall conductivity of the amorphous material can be assessed by means of the Kubo-Bastin formalism for periodic solids, making use of the local atomic arrangement. By comparison with calculations for the fcc, bcc, and hcp structures, we conclude that the local atomic arrangement in the amorphous W-Hf is most likely of the bcc type. We predict that a bcc solid solution of $W_{0.9}Hf_{0.1}$ has a particularly large spin Hall conductivity. However, in the experiment no such peak is observed, in agreement with the result that no homogenous solid solution is formed in sputtered W-Hf films at this composition. By means of a low-energy deposition technique such as molecular beam epitaxy (MBE) it might be possible to enforce the formation of a solid solution despite its positive formation enthalpy and thus obtain a material with a very high (negative) spin Hall conductivity. Because amorphous materials contain no grains, these may become an experimental platform for pinning-free Skyrmion dynamics [44], where the Skyrmions are efficiently manipulated by the large spin Hall effect. This work demonstrates the utility of first principles calculations of the spin Hall conductivity for a rational materials design of novel intermetallic systems with large spin Hall angles.

APPENDIX

1. Harmonic Hall analysis

In Fig. 4 we exemplarily show the dependence of the planar harmonic Hall analysis on the external field strength. The in-phase first harmonic signal V_ω (4) shows the usual $\sin 2\varphi$ behavior. At large magnetic field, a small $\sin(\varphi + \varphi_0)$ component is superimposed, which arises from a slight misalignment of the magnetic field: the out-of-plane component of the field induces a small $\sin(\varphi)$-like anomalous Hall contribution to the Hall voltage. In our analysis, this contribution is neglected. For the harmonic Hall analysis, the misalignment can also be safely neglected, because the second harmonic response does not change for a small out-of-plane misalignment of the
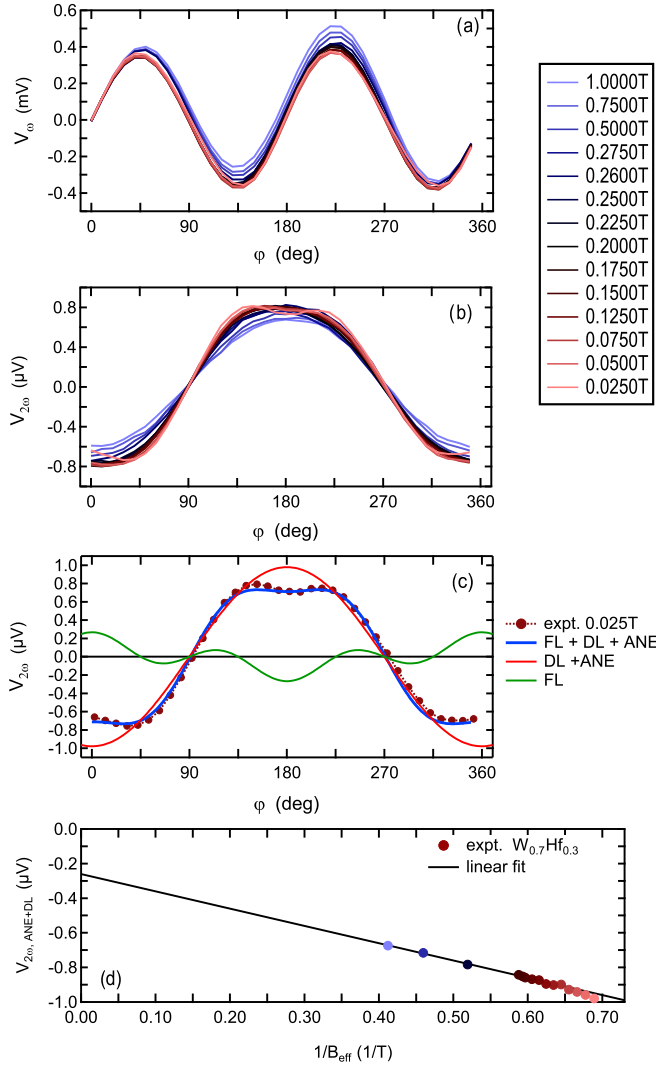
FIG. 4. (a) First harmonic in-phase signal of $W_{0.7}Hf_{0.3}$ for different in-plane magnetic fields. (b) Corresponding second harmonic out-of-phase signals. (c) Example analysis of the second harmonic Hall voltage and fit of Eq. (1). (d) Dependence of the second-harmonic voltage $\cos(\varphi)$ (DL + ANE) contribution on the reciprocal effective field. Errors are smaller than the symbol size.

magnetization $[V_{2\omega} \propto dV_\omega/d\theta_B = R_A I \sin(\theta_B) = \text{const}$ for $\theta_B = \pi/2 \pm \Delta\theta_B]$ [33]. The out-of-phase second harmonic signal $V_{2\omega}$ is composed of two contributions, the field-like (FL) and the dampinglike/anomalous Nernst (DL+ANE) term in Eq. (1). As predicted by the equation, the FL term vanishes approximately as $1/B_{\text{ext}}$, whereas the DL vanishes as $1/B_{\text{eff}}$, and the ANE contribution is independent of the magnetic field strength. This can be seen in Fig. 4(b), where the FL contribution vanishes quickly with increasing external field and a cosinusoidal curve remains, the amplitude of which vanishes slowly with the external magnetic field. By fitting Eq. (1) to the data, the two FL and DL+ANE contributions can be cleanly distinguished, as is shown in Fig. 4(c). By plotting the magnitude of the DL+ANE component as a function of $1/B_{\text{eff}}$, we obtain the data shown in Fig. 4(d). A line fit to the high-field portion of the data allows determining the DL and ANE contributions, from which α' and B_{DL} are calculated.

2. Error analysis and statistics

The fit shown in Fig. 4(c) is obtained from a least-squares minimization using the Levenberg-Marquardt algorithm. The target function to be minimized is

$$\chi^2(\boldsymbol{a}) = \sum_{i=1}^{M} \frac{1}{\sigma_i^2}[y_i - f(x_i, \boldsymbol{a})]^2, \tag{A1}$$

where M is the number of data pairs (x_i, y_i), σ_i^2 is the variance of the probability distribution function of the error at x_i, f is the fit function, and $\boldsymbol{a} = (a_1, \dots, a_N)$ is the parameter vector of the fit function. The error of the optimized parameter a_{0j} is given by $\sigma_{a_{0j}}^2 = c_{jj}$, where c_{jj} are the diagonal elements of the covariance matrix $\boldsymbol{C}$. The latter is calculated from the inverse of the Hessian matrix $\boldsymbol{H}$ of χ^2 with respect to the parameters, which has the matrix elements

$$h_{jk}(\boldsymbol{a}_0) = \frac{1}{2}\frac{\partial^2 \chi^2(\boldsymbol{a})}{\partial a_j \partial a_k}\bigg|_{\boldsymbol{a}_0}. \tag{A2}$$

Here, $\boldsymbol{a}_0$ is the parameter vector minimizing χ^2. Because the variances σ_i^2 are not known, the covariance matrix is obtained by scaling to the reduced χ^2 after the fit, i.e.,

$$\boldsymbol{C} = \boldsymbol{H}^{-1}\frac{\chi^2(\boldsymbol{a}_0)}{M - N}. \tag{A3}$$

In other words, the values of σ_i^2 are scaled to match the sample variance of the residuals $[y_i - f(x_i, \boldsymbol{a}_0)]$ after the fit and are used as an estimator for the variance of the underlying probability distribution. As the starting value, we chose $\sigma_i = 1 \forall i$ without any restrictions. Following the same scheme as described above, line fits were performed to the data as shown in Fig. 4(d) and parameter errors were estimated. This procedure led to a value of θ_{SH} and α' for each Hall cross on the samples under investigation. To obtain the average of several Hall crosses per sample properly accounting for different levels of noise on the raw data, we performed inverse-variance weighted means. Consider a set of n independent measurements of the same quantity Y with values and errors $y_i \pm \sigma_i$. Then the inverse-variance weighted mean is

$$\mu = \frac{\sum_{i=1}^{n} w_i y_i}{\sum_{i=1}^{n} w_i}, \quad w_i = \frac{1}{\sigma_i^2}. \tag{A4}$$

Accordingly, the inverse-variance weighted sample variance is obtained as

$$\hat{\sigma}_\mu^2 = \frac{\sum_{i=1}^{n} w_i(y_i - \mu)^2}{\sum_{i=1}^{n} w_i}. \tag{A5}$$

Following this procedure, the quantities and their error estimates shown in Fig. 2 were obtained, wherein the parameter errors from the previous line fits [Fig. 4(d)] were taken as weights for the averages. This procedure ensures that data points with large parameter errors from the least-squares fitting have smaller weight in the average than data points originating from raw data with better quality. For a more detailed discussion of the nonlinear fitting and statistical parameter estimation, we refer the reader to the standard literature on the subject.

Finally, we make a note on the large error bars for the pure bcc-W samples. Because of the low resistivity of bcc-W, only

a very small fraction of the current flows through the CoFeB layer, which results in tiny anomalous/planar Hall amplitudes. Since the second harmonic signal scales directly with these amplitudes, the measurement of $V_{2\omega}$ is very difficult and requires higher current density (because $V_{2\omega} \propto j^2$) and very long time constants in the lock-in measurements. Still, only

somewhat noisy data could be obtained. For an accurate measurement of the spin Hall conductivity of pure bcc-W, we suggest using a ferromagnet with similar resistivity. As this is not the main scope of the present manuscript, we accept the large uncertainty in the determination of the SHC of bcc-W.

[1] M. I. Dyakonov and V. I. Perel, Phys. Lett. A **35**, 459 (1971).

[2] J. E. Hirsch, Phys. Rev. Lett. **83**, 1834 (1999).

[3] A. Hoffmann, IEEE Trans. Magn. **49**, 5172 (2013).

[4] J. Sinova, S. O. Valenzuela, J. Wunderlich, C. H. Back, and T. Jungwirth, Rev. Mod. Phys. **87**, 1213 (2015).

[5] X. Qiu, P. Deorani, K. Narayanapillai, K.-S. Lee, K.-J. Lee, H.-W. Lee, and H. Yang, Sci. Rep. **4**, 4491 (2014).

[6] E. Sagasta, Y. Omori, M. Isasa, M. Gradhand, L. E. Hueso, Y. Niimi, Y. C. Otani, and F. Casanova, Phys. Rev. B **94**, 060412 (2016).

[7] M.-H. Nguyen, D. C. Ralph, and R. A. Buhrman, Phys. Rev. Lett. **116**, 126601 (2016).

[8] T. Schulz, K. Lee, B. Krüger, R. Lo Conte, G. V. Karnad, K. Garcia, L. Vila, B. Ocker, D. Ravelosona, and M. Kläui, Phys. Rev. B **95**, 224409 (2017).

[9] W. Zhang, W. Han, X. Jiang, S.-H. Yang, and S. S. P. Parkin, Nat. Phys. **11**, 496 (2015).

[10] T. Tanaka, H. Kontani, M. Naito, T. Naito, D. S. Hirashima, K. Yamada, and J. Inoue, Phys. Rev. B **77**, 165117 (2008).

[11] F. Freimuth, S. Blügel, and Y. Mokrousov, Phys. Rev. Lett. **105**, 246602 (2010).

[12] S. Lowitzer, M. Gradhand, D. Ködderitzsch, D. V. Fedorov, I. Mertig, and H. Ebert, Phys. Rev. Lett. **106**, 056601 (2011).

[13] M. Gradhand, D. V. Fedorov, F. Pientka, P. Zahn, I. Mertig, and B. L. Györffy, J. Phys.: Condens. Matter **24**, 213202 (2012).

[14] D. Ködderitzsch, K. Chadova, and H. Ebert, Phys. Rev. B **92**, 184415 (2015).

[15] C.-F. F. Pai, L. Liu, Y. Li, H. W. Tseng, D. C. Ralph, and R. A. Buhrman, Appl. Phys. Lett. **101**, 122404 (2012).

[16] L. Liu, C.-F. Pai, Y. Li, H. W. Tseng, D. C. Ralph, and R. A. Buhrman, Science **336**, 555 (2012).

[17] M. Obstbaum, M. Decker, A. K. Greitner, M. Haertinger, T. N. G. Meier, M. Kronseder, K. Chadova, S. Wimmer, D. Ködderitzsch, H. Ebert, and C. H. Back, Phys. Rev. Lett. **117**, 167204 (2016).

[18] M.-H. Nguyen, M. Zhao, D. C. Ralph, and R. A. Buhrman, Appl. Phys. Lett. **108**, 242407 (2016).

[19] A. Manchon and S. Zhang, Phys. Rev. B **79**, 094422 (2009).

[20] L. Liu, C.-F. Pai, D. C. Ralph, and R. A. Buhrman, Phys. Rev. Lett. **109**, 186602 (2012).

[21] I. Mihai Miron, G. Gaudin, S. Auffret, B. Rodmacq, A. Schuhl, S. Pizzini, J. Vogel, and P. Gambardella, Nat. Mater. **9**, 230 (2010).

[22] I. M. Miron, K. Garello, G. Gaudin, P.-J. Zermatten, M. V. Costache, S. Auffret, S. Bandiera, B. Rodmacq, A. Schuhl, and P. Gambardella, Nature (London) **476**, 189 (2011).

[23] M. Cubukcu, O. Boulle, M. Drouard, K. Garello, C. Onur Avci, I. Mihai Miron, J. Langer, B. Ocker, P. Gambardella, and G. Gaudin, Appl. Phys. Lett. **104**, 042406 (2014).

[24] K. Garello, C. O. Avci, I. M. Miron, M. Baumgartner, A. Ghosh, S. Auffret, O. Boulle, G. Gaudin, and P. Gambardella, Appl. Phys. Lett. **105**, 212402 (2014).

[25] S. Fukami, C. Zhang, S. DuttaGupta, A. Kurenkov, and H. Ohno, Nat. Mater. **15**, 535 (2016).

[26] Y.-C. Lau, D. Betto, K. Rode, J. M. D. Coey, and P. Stamenov, Nat. Nanotechnol. **11**, 758 (2016).

[27] G. Prenat, K. Jabeur, P. Vanhauwaert, G. Di Pendina, F. Oboril, R. Bishnoi, M. Ebrahimi, N. Lamard, O. Boulle, K. Garello, J. Langer, B. Ocker, M.-C. Cyrille, P. Gambardella, M. Tahoori, and G. Gaudin, IEEE Trans. Multi-Scale Comput. Syst. **2**, 49 (2016).

[28] F. Oboril, R. Bishnoi, M. Ebrahimi, and M. B. Tahoori, IEEE Trans. Comput. Des. Integr. Circuits Syst. **34**, 367 (2015).

[29] K.-U. Demasius, T. Phung, W. Zhang, B. P. Hughes, S.-H. Yang, A. Kellock, W. Han, A. Pushp, and S. S. P. Parkin, Nat. Commun. **7**, 10644 (2016).

[30] L. Neumann, D. Meier, J. Schmalhorst, K. Rott, G. Reiss, and M. Meinert, Appl. Phys. Lett. **109**, 142405 (2016).

[31] A. C. Lieser, C. L. Zacherl, A. Saengdeejing, Z. K. Liu, and L. J. Kecskes, Calphad **38**, 92 (2012).

[32] Y. Wen, J. Wu, P. Li, Q. Zhang, Y. Zhao, A. Manchon, J. Q. Xiao, and X. Zhang, Phys. Rev. B **95**, 104403 (2017).

[33] C. O. Avci, K. Garello, M. Gabureac, A. Ghosh, A. Fuhrer, S. F. Alvarado, and P. Gambardella, Phys. Rev. B **90**, 224427 (2014).

[34] We note that the equations for the harmonic Hall resistance in Ref. [33] suggest that $V_{2\omega,\text{ANE}} \propto I_0^2 \nabla T$, which is not correct. Here we rewrite the equations in the correct form.

[35] K. Garello, I. M. Miron, C. O. Avci, F. Freimuth, Y. Mokrousov, S. Blügel, S. Auffret, O. Boulle, G. Gaudin, and P. Gambardella, Nat. Nanotechnol. **8**, 587 (2013).

[36] L. Neumann and M. Meinert, AIP Adv. **8**, 095320 (2018).

[37] H. Ebert, S. Mankovsky, K. Chadova, S. Polesya, J. Minár, and D. Ködderitzsch, Phys. Rev. B **91**, 165132 (2015).

[38] H. Ebert, D. Ködderitzsch, and J. Minár, Rep. Prog. Phys. **74**, 096501 (2011).

[39] H. Ebert *et al.*, *The Munich SPR-KKR package*, version 7.7, http://olymp.cup.uni-muenchen.de/ak/ebert/SPRKKR.

[40] A. Jain, S. P. Ong, G. Hautier, W. Chen, W. D. Richards, S. Dacek, S. Cholia, D. Gunter, D. Skinner, G. Ceder, and K. A. Persson, APL Mater. **1**, 011002 (2013).

[41] S. Xiong, W. Qi, B. Huang, M. Wang, and L. Wei, J. Phys. Chem. C **115**, 10365 (2011).

[42] T. Seifert, S. Jaiswal, U. Martens, J. Hannegan, L. Braun, P. Maldonado, F. Freimuth, A. Kronenberg, J. Henrizi, I. Radu, E. Beaurepaire, Y. Mokrousov, P. M. Oppeneer, M. Jourdan, G. Jakob, D. Turchinovich, L. M. Hayden, M. Wolf, M. Münzenberg, M. Kläui, and T. Kampfrath, Nat. Photon. **10**, 483 (2016).

[43] D. Choi, C. S. Kim, D. Naveh, S. Chung, A. P. Warren, N. T. Nuhfer, M. F. Toney, K. R. Coffey, and K. Barmak, Phys. Rev. B **86**, 045432 (2012).

[44] W. Legrand, D. Maccariello, N. Reyren, K. Garcia, C. Moutafis, C. Moreau-Luchaire, S. Collin, K. Bouzehouane, V. Cros, and A. Fert, Nano Lett. **17**, 2703 (2017).